Characterization of surface clutter signal in presence of orography for a spaceborne conically scanning W-band Doppler radar

Francesco Manconi[1], Alessandro Battaglia[1,2], and Pavlos Kollias[3,4]

[1]DIATI, Politecnico of Torino, Turin, Italy
[2]Department of Physics and Astronomy, University of Leicester, Leicester, UK
[3]School of Marine and Atmospheric Sciences, Stony Brook University, Stony Brook, NY, USA
[4]Department of Atmospheric and Oceanic Sciences, McGill University, Montreal, QC Canada

Correspondence: francesco.manconi@polito.it

Abstract. The Earth's surface radar reflection is one of the most important signals received by spaceborne radar systems. It is used in several scientific applications including geolocation, terrain classification, and path-integrated attenuation estimation. A simulator based on the ray tracing approach has been developed to reproduce the clutter reflectivity and the Doppler velocity signal for a conically scanning spaceborne Doppler radar system. The simulator exploits topographic information through a raster Digital Elevation Model, land types from a regional classification database, and a normalized radar surface cross-section look-up table. The simulator is applied to the WInd VElocity Radar Nephoscop (WIVERN) mission, which proposes a conically scanning W-band Doppler radar to study in-cloud winds. Using an orbital model, detailed simulations for conical scans over the Piedmont region of Italy that offers a variety of landscape conditions are presented. The results highlight the strong departure of the reflectivity and Doppler velocity profiles in the presence of marked orography and the significant gradient in the surface radar backscattering properties. The simulations demonstrate the limitations and advantages of using the surface Doppler velocity over land as an antenna-pointing characterization technique. The simulations represent the full strength range of the surface radar clutter over land surfaces for the WIVERN radar. The surface clutter tool applies to other spaceborne radar missions such as the nadir pointing EarthCARE and CloudSat cloud profiling radars, or thecross-track scanning GPM precipitation radars.

1 Introduction

Space-borne atmospheric radars in bands between X and G (i.e. from 10 to 300 GHz) are now considered cornerstones of the global observing system for characterising vertical profiles of clouds and precipitation systems (Battaglia et al., 2020). While Ku-Ka and W bands have been used in space for more than a decade (Kummerow et al., 1998; Skofronick-Jackson et al., 2016; Stephens et al., 2018; Illingworth et al., 2015), new frequency bands are currently being explored (Battaglia et al., 2014; Li et al., 2020), with novel scanning modes (e.g. conical scanning as proposed in Illingworth et al. (2018)) and innovative Doppler capabilities (Battaglia et al., 2013; Tanelli et al., 2016; Kollias et al., 2022). Compared to ground-based radars, space-based radars provide a global perspective and are particularly well suited to studying clouds in the upper troposphere, where attenuation by water vapour and liquid-phase hydrometeor is less pronounced. Conversely, space-based observations are hampered

by the strong surface return (hereafter referred to as "clutter") that tends to obscure the hydrometeor signal near the ground.
Knowing the shape of the clutter reflectivity allows the signal to clutter ratio to be determined. This parameter is an indication of the "blind zone" near the surface and is crucial for the correct quantification of surface precipitation (Maahn et al., 2014), the detection of shallow clouds (Burns et al. (2016); Lamer et al. (2020)) and the measurement of near-surface winds. Meneghini and Kozu (1990) suggested that the blind zone can be significantly reduced when scanning at high angles of incidence (similar to scatterometers) due to the reduced surface normalised radar cross section (NRCS) when moving away from the nadir looking configuration.

The WIVERN mission, short for WInd VElocity Radar Nephoscope, www.wivern.polito.it (Illingworth et al., 2018; Battaglia et al., 2022; ESA-WIVERN-Team, 2023), one of the two remaining candidates in ESA's Earth Explorer 11 programme, proposes a W-band conically scanning radar with an angle of incidence of about 42°. It is therefore timely to investigate and assess how beneficial such a scanning configuration could be in terms of reducing the signal-to-clutter ratio.

On the other hand, the presence of the surface return represents an opportunity because it provides a reference point that can be used either to derive the path integrated attenuation via the surface reference technique (Meneghini et al., 2000), to calibrate the reflectivity (Tanelli et al., 2008) and/or the Doppler velocity (Battaglia and Kollias, 2014; Scarsi et al., 2024) and/or to provide accurate geolocation (Puigdomènech Treserras and Kollias, 2024). In particular, based on simulations for flat homogeneous surfaces for the WIVERN radar specifics, Scarsi et al. (2024) showed that the clutter Doppler velocity profiles (expected to be 0 m/s in correspondence to the surface reflectivity peak) can be used for mispointing corrections. However, in presence of real land surfaces, clutter Doppler velocity and reflectivity profiles are expected to deviate significantly for two reasons:

1. the variability of surface height within the radar footprint introduced by the orography, which will alter the iso-range lines;

2. the inhomogeneity of the surface backscatter cross section within the radar footprint (the so called non uniform beam filling, NUBF, Tanelli et al. (2002)), that will bias the Doppler velocity signal towards the velocities of the brightest regions.

The aim of this work is to extend the simulations of the clutter signal to non-planar surfaces (characterised by a very high resolution DEM), including a realistic variability of the surface backscatter (based on a surface classification index). A geometric-optical approach is used, similar to that used in Delrieu et al. (1995); Gabella and Perona (1998); Gabella et al. (2008) for ground-based weather radars. The novelty is the application to a space-based configuration, the extension to the Doppler signal and the inclusion of NUBF effects. The simulator will be applied to several case studies and an initial assessment will be made of how much the shape of the reflectivity and Doppler velocity profiles are distorted from those expected for a flat homogeneous surface.

After introducing the methodology (Sect. 2), examples of the simulation are illustrated in Sect. 3 for an overpass over the mountainous Piedmont region (northwest part of Italy). Finally a statistical analysis is presented in Sect. 4. Conclusions and future work are outlined in Sect. 5.
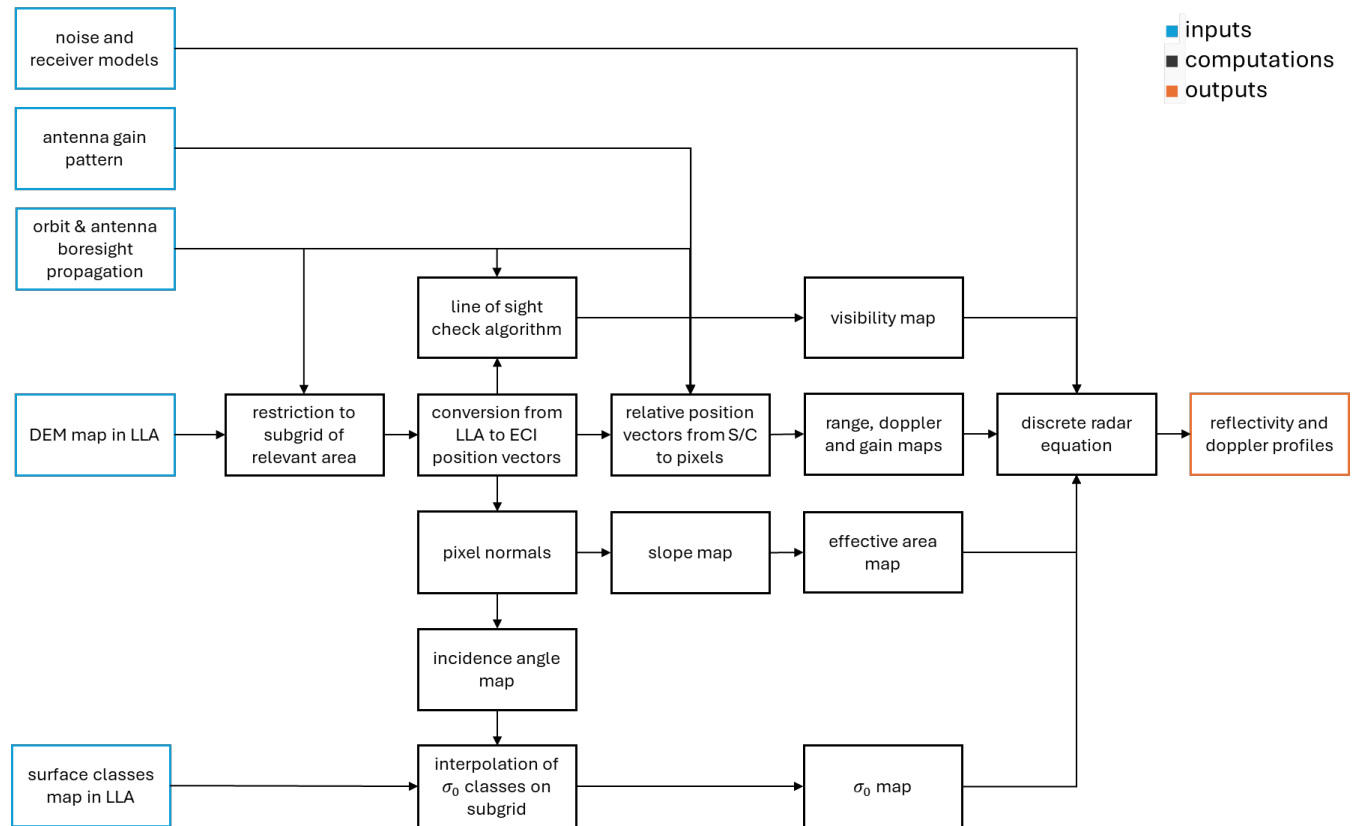
Figure 1. Flowchart of ground clutter computation code flowchart. LLA= latitude, longitude and altitude; ECI=Earth centered inertial.

2 Methodology

The flowchart of the procedure that computes the surface clutter signal (reflectivity and Doppler velocity) is presented in Fig. 1.

60 The software inputs are: 1) a raster Digital Elevation Model (DEM) map; 2) a surface class map; 3) the satellite orbit with the associated antenna scanning; 4) the antenna gain pattern; 5) a noise and receiver model. These inputs are used to compute the two oclutter reflectivity and Doppler velocity profiles.
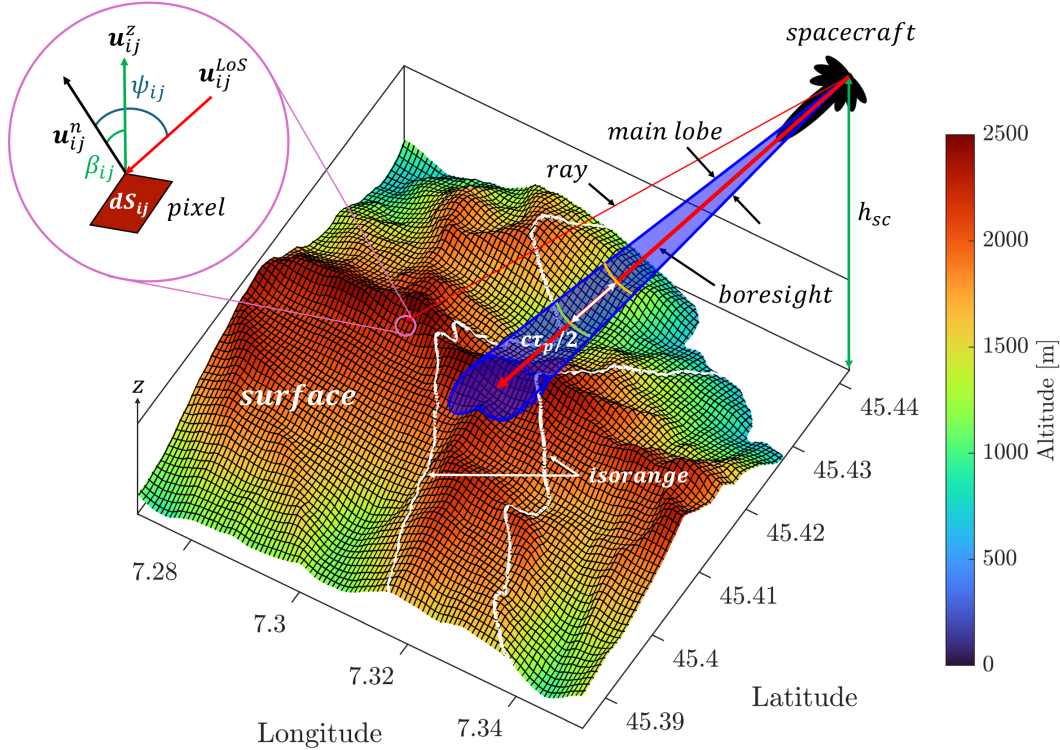
Figure 2. Geometry for a slant-looking radar illuminating a region with pronounced orography described by a high resolution DEM. The reflectivity and Doppler velocity at any given range r are computed via an integral extended to the region comprises between $r - c\tau_p/4$ and $r + c\tau_p/4$ as described in Sect. 2.1 (Eqs. 4-6). Such surface region is divided in infinitesimal elements (black squares). All the relevant mathematical quantities are illustrated in the top left inset. The two white isoranges in the figure correspond to $r_{bs} - c\tau_p/4$ and $r_{bs} + c\tau_p/4$, where r_{bs} is the range in the boresight direction.

2.1 Surface echo return: reflectivity and Doppler velocity

Fig. 2 shows the geometry for slant angle radar observations, where a pulse hits the surface at an angle of incidence, θ_{inc}. It is

65   assumed that the transmitted radar pulse has a top hat shape with a duration of τ_p and is transmitted according to an antenna pattern characterised by a main lobe (blue shaded cone) and various side lobes (black envelopes). Iso-range lines are shown on the illuminated orographic surface, one for the leading edge and one for the trailing edge of the top-hat pulse shape around the range of the intersection between the boresight axis and the DEM surface. WIVERN orbit and radar specifics are listed in Tab. 1.

70   The power received at any time t (and the corresponding range $r = ct/2$, where c is the speed of light) results from the contributions of targets located within the spheres centred on the radar and produced by the propagation of the trailing and leading edges of the pulse, shown in Fig. 2 as orange and green curves respectively. In the case of a flat surface, these targets include an annular strip of terrain (Battaglia et al. (2017)), but in the case of complex terrain such regions, identified in the

Table 1. WIVERN orbit and radar specifics, as currently under study in the Phase-A study for the ESA Earth Explorer 11 program.

Spacecraft height, h_{SC}	500 km
Spacecraft velocity, v_{SC}	7600 ms^{-1}
Orbit inclination, i	97.42°
Orbit Local Time of the ascending node, $LTAN$	06:00
Incidence angle, θ_{inc}	41.6°
Swath width at ground	800 km
Radar output frequency	94.05 GHz
Pulse width τ	3.3 μs
Antenna angular velocity, Ω_a	12 rpm
Antenna elevation beamwidth, θ_{3dB}	0.0656 deg
Antenna azimuth beamwidth, ϕ_{3dB}	0.0722 deg
Footprint speed	500 kms^{-1}
Single pulse minimum detectable reflectivity	-18 dBZ
H-V Pair Repetition Frequency	4 kHz
Range sampling distance (rate)	100 m (1.5 MHz)
Number of H-V Pairs per 1 km integration length	8

following as S, become much more complicated and dependent on the illumination geometry and the orography. The power received by the radar from the surface at range r, P_r, assuming that the antenna gain is identical for transmission and reception, is given by an integration performed over the illuminated area, S (Meneghini and Kozu, 1990):

$$P_r(r) = \underbrace{\left[P_t \frac{\lambda^2}{(4\pi)^3} G_0^2 \right]}_{C_S} \int_S \frac{\sigma_0(\psi)\, G_n^2\, |u(t - 2r/c)|^2}{r^4}\, dS \approx C_S \sum_{i,j} \frac{\sigma_0(\psi_{ij})\, G_n^2(\mathbf{u}_{ij}^{LoS})\, |u(t - 2r_{ij}/c)|^2}{r_{ij}^4} dS_{ij} \tag{1}$$

where P_t is the transmitted power, λ is the wavelength of radar, $G = G_0 G_n$ is the antenna gain (G_0 being the maximum gain at antenna boresight), $u(t)$ is the complex voltage envelope of the transmitted pulse (for a top hat shape $|u(t)| = 1$ for $0 < t < \tau_p$), ψ is the local incidence angle that can be computed as $\psi = acos(\mathbf{u}_{ij}^{LoS} \cdot \mathbf{u}_{ij}^n)$ where $\mathbf{u}_{ij}^n$ is the normal to the infinitesimal surface. The integral (summation) is extended only to those pixels that are visible from the radar (see Sect. 2.1.1). The normalised radar cross section ($NRCS$), σ_0, is defined as the surface radar backscatter cross section, σ_{surf}^{back} normalised to the surface area, A, and is typically expressed in dB units as:

$$\sigma_0[dB] \equiv 10 \log_{10} \frac{\sigma_{surf}^{back}}{A}. \tag{2}$$

No attenuation effect has been included. On the right hand side of Eq. (1) the integral has been replaced by a summation over different small surfaces. $\mathbf{u}_{ij}^{LoS}$ is the line-of-sight unit vector joining the satellite to the surface element. Note that a radar constant C_S relevant for a surface target has been introduced (square bracket in Eq. 1).

The area dS_{ij} can be computed as a function of the DEM pixel area $\Delta x_i \, \Delta y_j$ by:

$$dS_{ij} = \frac{\Delta x_i \, \Delta y_j}{\cos(\beta_{ij})}$$

90 where β_{ij} is the slope of the ij surface element that can be derived as $\beta = acos(\mathbf{u}_{ij}^z \cdot \mathbf{u}_{ij}^n)$ where $\mathbf{u}_{ij}^z$ is the unit vector along the local vertical direction.

In radar meteorology for meteorological distributed targets the radar reflectivity is defined as:

$$P_r(r) = C_M \frac{Z}{r^2} \qquad \text{where} \quad C_M \equiv \frac{\pi^2}{2^6} \frac{P_t \, G_0^2 \Omega_{2A}}{\lambda^2} \frac{c\tau_p}{2} |K_w|^2 = C_S \frac{\pi^5 |K_w|^2 \Omega_{2A}}{\lambda^4} \frac{c\tau_p}{2} \tag{3}$$

where K_w is derived from the refractive index of water at 3 mm-wavelengths ($|K_w|^2$ assumed equal to 0.78), $\Omega_{2A} \equiv \int G_n^2 d\Omega$

95 (which for a Gaussian beam is approximately equal to $\frac{\pi \theta_{3dB} \phi_{3dB}}{8 \log(2)}$) and C_S is another radar constant, previously defined in Eq. (1). Eq. (3) allows to convert P_r to Z_e for any given range as:

$$Z(r) = r^2 \frac{2\lambda^4}{\pi^5 |K_w|^2 \Omega_{2A} c\tau_p} \sum_{i,j} \frac{\sigma_0(\psi_{ij}) \, G_n^2(\mathbf{u}_{ij}^{LoS}) \, |u(t - 2r_{ij}/c)|^2}{r_{ij}^4} dS_{ij}. \tag{4}$$

Note that for flat surfaces with constant NRCS, σ_0:

$$\int Z(r) dr = \frac{\lambda^4 \sigma_0}{\pi^5 |K_w|^2 \cos\theta_{inc}} \tag{5}$$

100 which provides a useful check for the normalization of the reflectivity profile.

The Doppler velocity at range r is computed similarly to Eq. (4) as:

$$v_D(r) = \frac{C_S}{P_r(r)} \sum_{i,j} \frac{v_{SC}(ij)\sigma_0(\psi_{ij}) \, G_n^2(\mathbf{u}_{ij}^{LoS}) \, |u(t - 2r_{ij}/c)|^2}{r_{ij}^4} \, dS_{ij} \equiv \sum_{i,j} v_{SC}(ij) w_{ij}^v \tag{6}$$

where $v_{SC}(ij) = \mathbf{u}_{ij}^{LoS} \cdot \mathbf{v}_{SC}$ is the projection of the satellite velocity along the line-of-sight axis.

2.1.1 Surface DEM and visibility algorithm

The Advanced Spaceborne Thermal Emission and Reflection Radiometer (ASTER) Global Digital Elevation Model (GDEM) (https://asterweb.jpl.nasa.gov/GDEM.asp, Abrams et al. (2010)) provides finely resolved ($1'' \times 1''$, i.e. 30.9 m $\times$ 30.9 m at the equator) global topography maps. In this work, we focused on the Piedmont region, which is located in the NW of Italy and is of particular interest for the orography associated with the Western Alps on the border with France. From the geolocated elevation data it is possible to derive useful quantities such as the distance between the satellite and the different elementary surfaces dS_{ij} and the corresponding unit vector $\mathbf{u}_{ij}^{LoS}$ but also the two other unit vectors $\mathbf{u}_{ij}^n$ and $\mathbf{u}_{ij}^z$ previously defined (see inset in Fig. 2). Each pixel position, defined by the north-west vertex, is identified with latitude, longitude and altitude (LLA) coordinates in the WGS84 reference frame, and can be transformed from LLA to cartesian ECI coordinates $r_{i,j}^{ECI}$; for this step, assumption of a spherical Earth is used. The normal to each pixel, in general pointing outwards from the Earth surface, is found with the following relation:

$$\mathbf{u}_{i,j}^n = \left(\frac{\mathbf{r}_{i+1,j}^{ECI} - \mathbf{r}_{i,j}^{ECI}}{\|\mathbf{r}_{i+1,j}^{ECI} - \mathbf{r}_{i,j}^{ECI}\|} \right) \times \left(\frac{\mathbf{r}_{i,j+1}^{ECI} - \mathbf{r}_{i,j}^{ECI}}{\|\mathbf{r}_{i,j+1}^{ECI} - \mathbf{r}_{i,j}^{ECI}\|} \right)$$

with the indices i, j ordered, respectively, from north to south and from west to east.

In the integrals of Eqs. (4-6) pixels that are visible must be identified. Paths of the electromagnetic radiation propagating from the radar in all different directions within the antenna pattern are indicated as rays, and are assumed to be straight lines since bending is negligible at these viewing angles (Fabry, 2015). Visibility is checked iteratively for each ray connecting the spacecraft to the pixels of the considered DEM portion, up to a maximum altitude (which for this study was set to the maximum DEM regional value, 4564 m). Starting from each pixel and following such rays, range is decreased in small steps; then, altitude at the considered point is compared to the value obtained from interpolation of the DEM at the same horizontal coordinates. If the former is larger than the latter then the next iteration is performed; otherwise the visibility status is set to false and the iteration is aborted (see red ray in Fig. 3). If the maximum altitude is reached the visibility status is set to true and the ray tracing is terminated (see green ray in Fig. 3).
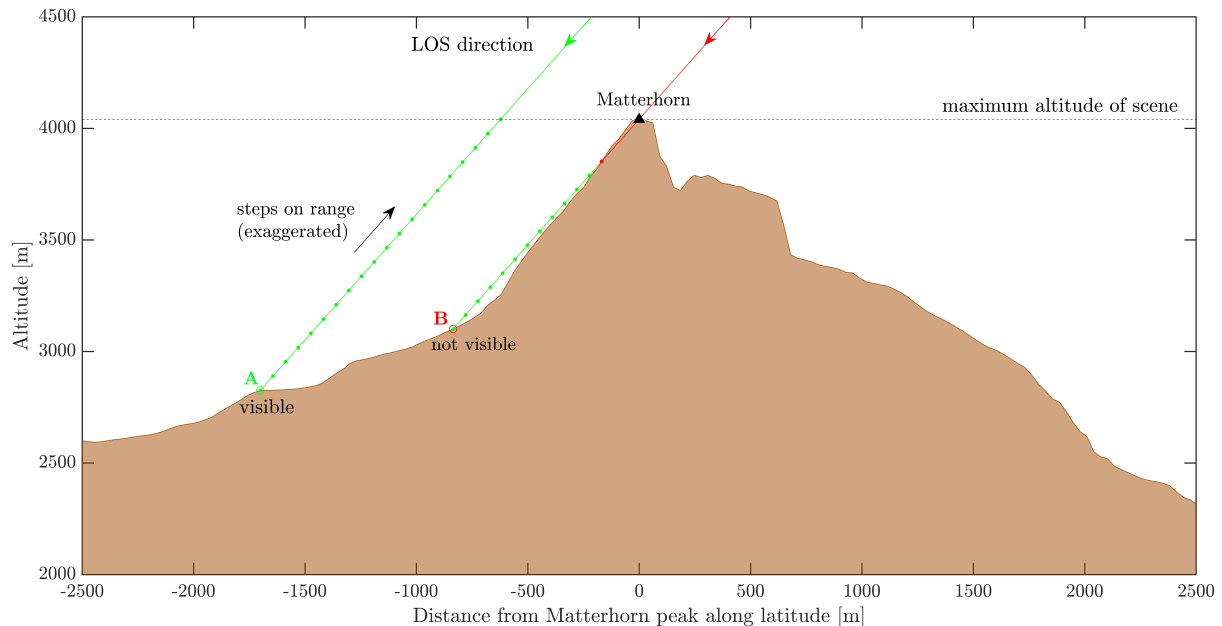
Figure 3. Schematic describing the idea underpinning the visibility algorithm with a longitudinal slice of a scene around the Matterhorn at a constant latitude of $44.667°$ E. For illustration purposes a red and a green ray are traced in proximity to the Matterhorn. Correspondingly point A (B) is (is not) visible. The dots correspond to the iterations done to check the visibility.

2.2 Terrain classification and NRCS

The other key element in the integrals of Eqs. (4-6) are the NRCSs. Ground-based field campaign measurements in the 90s for different land surfaces (Ulaby and Dodson, 1991) and more recent airborne measurements over water bodies (Battaglia et al., 2017; Wolde et al., 2019) have been used to create look-up-tables (LUTs). Seven surface types have been selected as representative of different NRCS behaviour (see list in Tab. 2) according to the available LUTs.
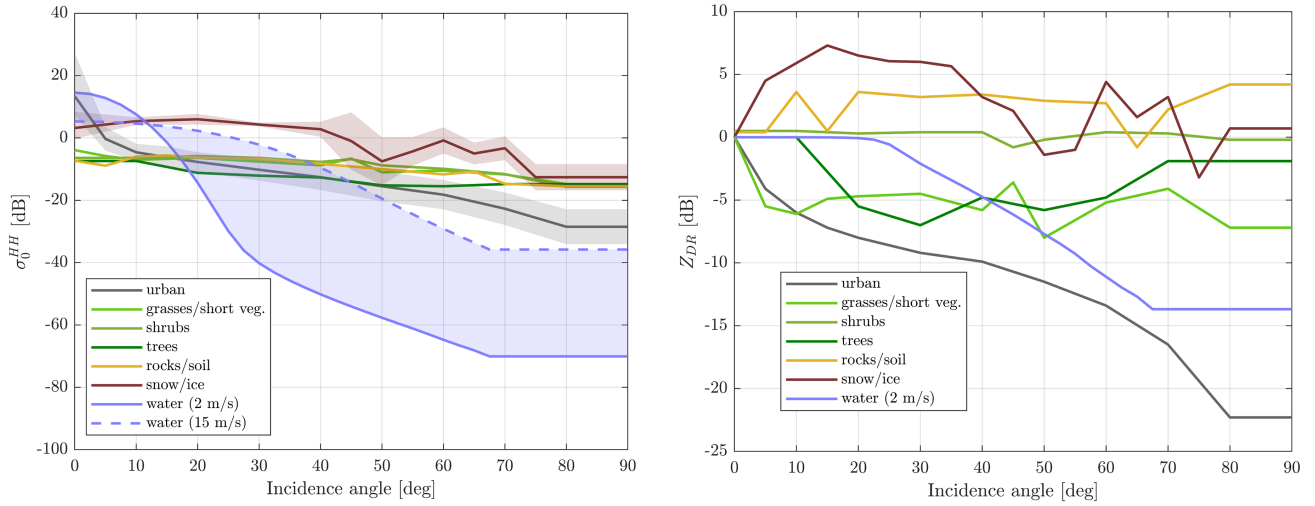
Figure 4. NRCS for H-polarised radiation, σ_0^{HH} (left) and linear depolarisation ratio $Z_{DR} \equiv \sigma_0^{HH} - \sigma_0^{VV}$ as a function of the incidence angle for the different surface types as used in this study (see Tab. 2). For two of the surface types the shaded area indicates the observed standard deviation.

The dependence of the NRCS for H-polarised radiation, σ_0^{HH} (left) and of linear depolarisation ratio $Z_{DR} \equiv \sigma_0^{HH} - \sigma_0^{VV}$ as a function of the incidence angle are shown in Fig. 4. Few remarks:

1. water surfaces have a strong dependence on the incidence angle with very strong surface dimming when moving towards high incidence angles;

2. land surfaces (with the exception of urban surfaces) show a much flatter response of the NRCS with the incidence angle with slight decreases with increasing incidence angles;

3. at about the WIVERN incidence angle land and ocean NRCSs vary in the range between 5 and -25 dB and between -15 and -50 dB, respectively;

4. close to nadir NRCSs vary broadly in the range between -10 and 20 dB in rough agreement with CloudSat measurements (Durden et al., 2011).

5. Z_{DR} are usually negative with few positive values in correspondence to rocks/soils and snow/ice.

A detailed surface classification map of the Piedmont area at 20 m resolution with dozens of classes has been provided by GEOPIEMONTE (https://geoportale.igr.piemonte.it/cms/). These terrain categories have been mapped into the seven classes listed in Tab. 2 for which a NRCS model was available and interpolated in the same grid as the DEM. The results for the Piedmont region is depicted in Fig. 5. Note the mountainous regions in the Western part at the border with France with mainly
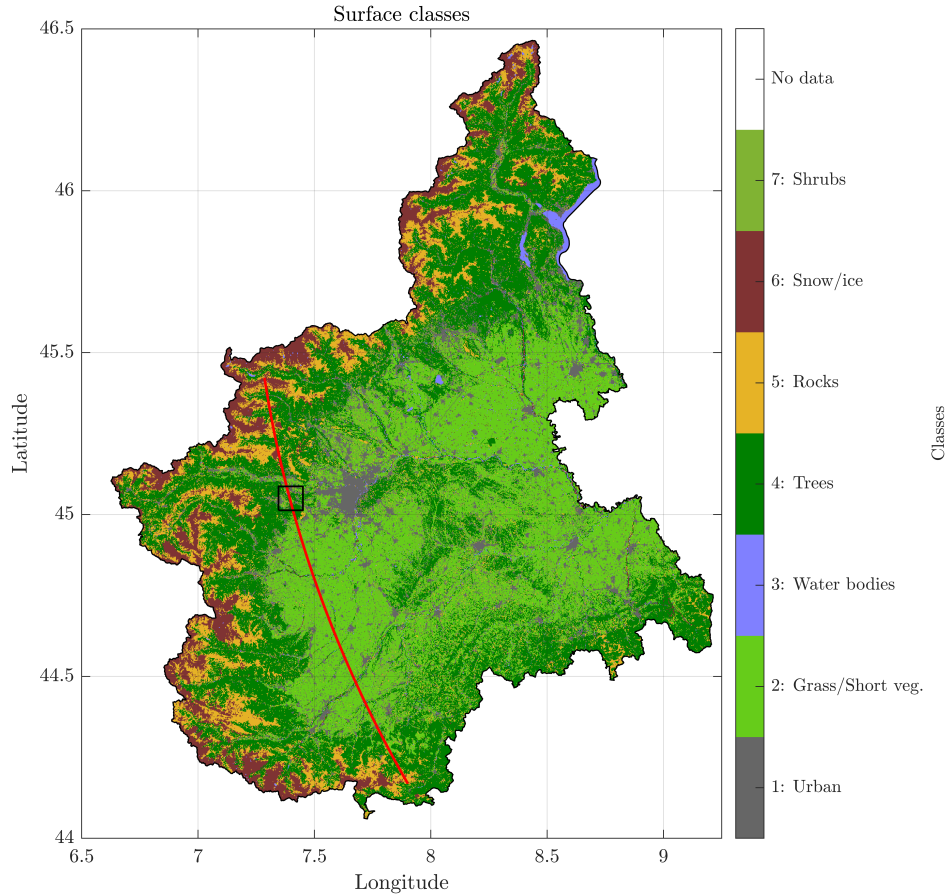
Figure 5. Terrain characterization of the Piedmont area (courtesy of Stefano Campus, GEOPIEMONTE). The red line represents the ground track of the antenna boresight for a case study scan (see Sect. 3.2). The black square corresponds to the region used in the single footprint case study in Sect. 3.1.

135 rocks, trees and snow/ice. This classification linked with the LUTs described in Sect. 2.2 allows computing the co-polar NRCSs at any given angle for H and V-polarised radiation.

2.3 Inclusion of noise and receiver response function

Once the ideal reflectivity, Doppler velocity and Doppler width profiles are computed according to Eqs. 4-6 at a range resolution of 50 m, real Doppler and reflectivity signals are generated according to the method proposed by Battaglia et al. (2024). This

140 takes into account the polarisation diversity (PD) (Battaglia et al., 2013) pulse sequence envisaged for WIVERN (Illingworth et al., 2018) with H and V pairs closely transmitted (with a separation of $20~\mu s$) and with PD pairs transmitted every $250~\mu s$ and the assumption that the pair repetition time is larger than the decorrelation time so that only pulses within the same polarisation diversity pair are correlated. The H and V pulses in each pairs have correlations computed in the approximation that spectra are

Table 2. List of surface types with an available NRCS model. Water is added to the six land surface categories present in the NRCS database as parameterised in Ulaby and Dodson (1991).

Number	Name
1	urban
2	grass/short vegetation
3	water bodies
4	trees
5	soil, rocks
6	snow/ice
7	shrubs

Gaussian with the given mean Doppler velocity and spectral width (Pazmany et al., 1999). Noise corresponding to a single pulse
145 -18 dBZ equivalent reflectivity is added to the signal. The I and Q are sampled every 50 m in range. Then they are convolved with a Hamming window to simulate the receiver response (Schutgens, 2008). Finally polarisation diversity pulse pair (PDPP) estimators (Battaglia et al., 2013, 2024) are used to compute the reflectivity and the mean Doppler velocity profiles.

An important consideration. Land surfaces are generally characterised by large values of linear depolarisation values and low values of ρ_{HV}, the correlation between H and V polarized signals. For the former (latter) values of the order of -10 to -3 dB
150 (0.4 to 0.8) are expected. While there is not much correlation for the co-polar surface signals there is an excellent correlation between the cross-polar signals generated by the surface (the so-called "surface ghosts" as discussed in Illingworth et al. (2018); Rizik et al. (2023) which appear above and below the surface and are separated in range by $2\Delta r_{T_{HV}}$ (Battaglia et al., 2024). These signals can then be used to extract the Doppler signal by performing a dedicated pulse pair processing that correlates the H and V profiles shifted by $2\Delta r_{T_{HV}}$. For such Doppler estimate, the reduction in signal-to-noise ratio (SNR) associated with
155 the surface linear depolarisation ratio is well compensated by the improvement in the Doppler estimators associated with the substantial increase in correlation. In the following two cases are considered:

1. a low correlation case ($\rho = 0.5$) but with the SNR expected from the σ_0 of the surfaces, representative of the standard PDPP processing;

2. a high correlation case ($\rho = 0.98$) but with the SNR reduced by 5 dB compared to the σ_0 of the surface in order to
160 account for the cross-talk. This case is representative of the Doppler estimates obtained by correlating the ghost signals.
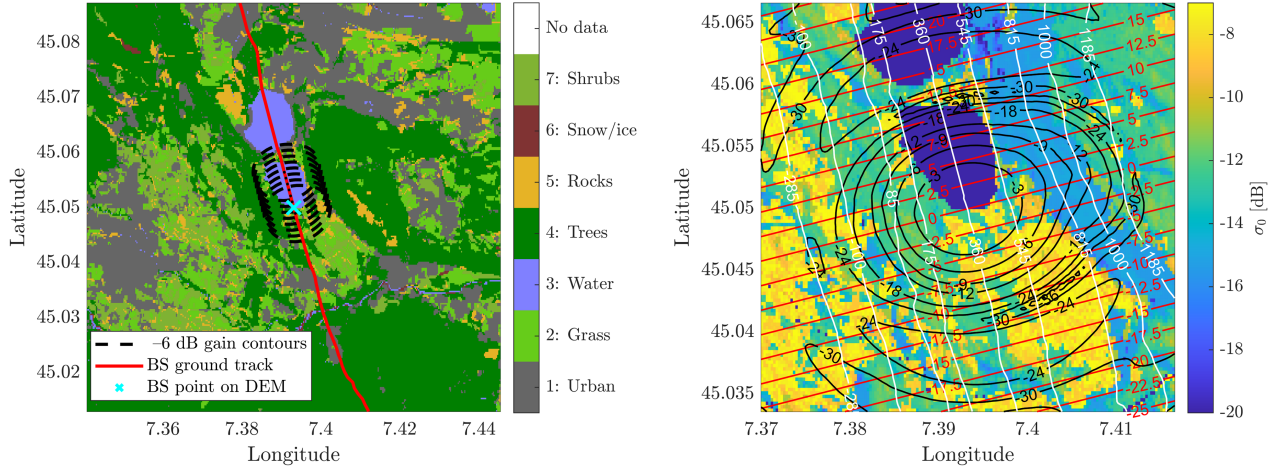
Figure 6. Case study with the WIVERN scanning ground track (red line) passing through the Western part of Piedmont region (see Fig. 5) with details of the terrain classes (left panel) and NRCS values (right panel). The profile with radar antenna boresight intercepting the DEM surface at the cyan cross near the Avigliana lakes (blue patches) is discussed in detail in the text. The right panel depicts all the relevant quantities that enter Eqs. (4-6) with the iso-range contours in white (converted to heights above the geoid), the iso-Doppler contours in red and the antenna iso-gain contours in black and the NRCS (color-coded); the colorbar has been clipped to a minimum value of -20 dB, but values over the wo lakes are very low (around -50 dB). Contours where the antenna gain is 6 dB lower than the maximum gain corresponding to the 8 footprints used to compute the 1 km averaging around the cyan cross are also shown in the left panel.

3 Case studies

3.1 Single footprint

A single footprint scene has been chosen as case study to illustrate the effect of NUBF (Figs. 6, 7, 8). The scene, with the radar in left side-looking configuration (antenna rotation angle measured clockwise from the satellite track direction or azimuth, ϕ_A, of about 270°), is centred over the Avigliana lakes, with the antenna boresight (bs) hitting the southern shore of the southernmost lake (black cross in the left panel of Fig. 6). The ideal (no noise, no receiver added) profiles for reflectivity and Doppler velocities are presented in Fig. 7. The reflectivity peaks at about 19 dBZ at an height of 360 m where the boresight hits the ground and then decreases below the -18 dBZ noise level at a height above sea level of about 1260 m and -250 m. In this case the clutter is more pronounced at ranges smaller than the range of the boresight (360 m); this is due to the presence of higher σ_0 values in correspondence to isoranges with $h > 360$ m (see right panel in Fig. 6). The Doppler profile on the other hand presents a very anomalous behaviour compared to the flat homogeneous terrain reference (red dashed line). In correspondence to the height of the boresight a negative Doppler velocity of -1.85 m/s is simulated. In fact near the center of the beam where the maximum antenna gain is achieved, pixels with negative Doppler velocities (contour lines in red) in the lower region have higher NRCS than the ones on the other half (see Fig. 6), as calm water bodies at about 41.6° present σ_0

175 values around -50 dB (see Fig. 4). This results in the negative Doppler bias around the height the boresight intercepts the DEM terrain. Conversely the two positive peaks observed at different altitudes (indicated as h_1 and h_2 in the right panel of Fig. 7) are due to the combined effect of the modified shape of the iso-range lines in presence of orography and of the antenna gain and σ_0 variability. This is highlighted in Fig. 8 where the weights defined in Eq. (6) are depicted for the three annuli that constitutes the area of integration for the three given heights. In correspondence of the two Doppler profile maxima (annuli labelled as

180 h_1 and h_2 in Fig. 7), pixels with positive velocities are characterised by higher antenna gain values than pixels with negative velocities; this converts in larger weights w_{ij}^v for $v_{SC}(ij) > 0$ and thus positive velocities overall.

In summary, two different effects can be seen. Along the central annulus, the water body has very low NRCS in the regions with positive Doppler values, resulting in a negative velocity bias. Inside the two lateral annuli of Fig. 8, the surface orography modifies the iso-range lines resulting in higher antenna gain values for pixels with positive velocity, with a positive bias at the

185 corresponding heights.
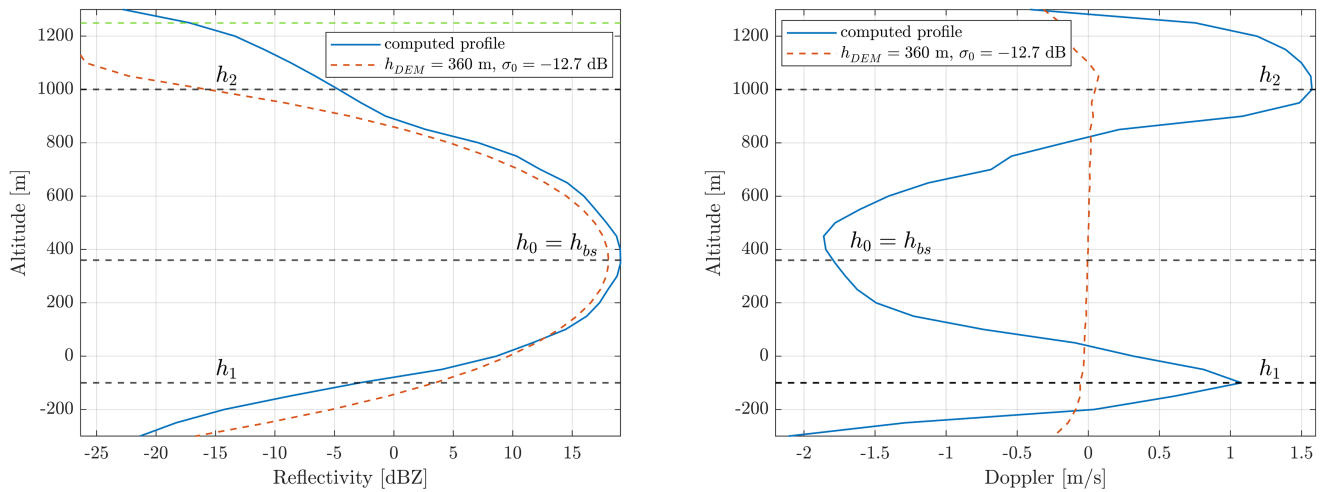
Figure 7. Case study for NUBF: reflectivity and Doppler profiles. Three heights have been selected, corresponding to peaks in the Doppler velocity profile (dashed horizontal black lines). The $h_0 = h_{bs}$ corresponds to the height of the point hit on the DEM by boresight axis. Ideal profiles in case of constant DEM height and constant NRCS equal to the local means are included. The green dotted line in the top of the left panel represents the height at which the profile drops below the single-pulse minimum detectable reflectivity of -18 dBZ, which corresponds to 1249 m in this case. Subtracting the boresight height (360 m), a -18 dBZ clutter depth of 889 m is obtained for this scene. This quantity will be explained in Sect. 4.1.
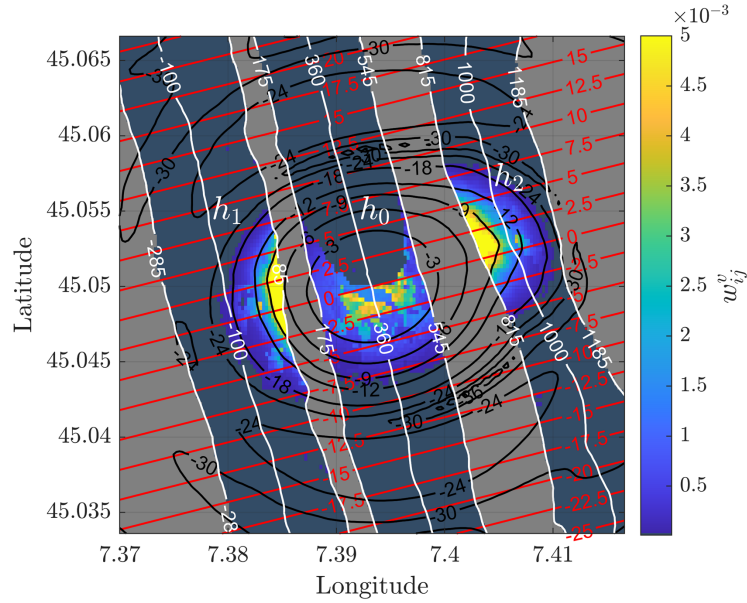
Figure 8. Case study for NUBF: map of the weights given to each pixel for computation of the Doppler velocity at a given height (see Eq. 6). The weights are defined as $w_{ij}^v = C_S P_r^{-1}(r_{ij}) \, \sigma_0(\psi_{ij}) \, G_n^2\left(u_{ij}^{LoS}\right) \, r_{ij}^{-4} \, dS_{ij}$ and are therefore dimensionless. Three heights corresponding to the peaks in the Doppler velocity profile have been selected; the three highlighted regions correspond to the surface domain that contributes to the integral in Eq. (6) for each of the the chosen heights (i.e. corresponds to ranges equal to the three given ranges $\pm 250 \, m$). Values fading to grey inside the annulus have magnitude lower than 10^{-5} and therefore can be neglected.

3.2 Scan

WIVERN (see Specs. in Tab. 1) will do conically scans moving the footprint at about 500 km/s and sending 8 pairs of H and V pulses every km. Therefore each footprint will be separated by 125 m along the boresight scanning track (e.g. see the black lines in the left panel of Fig. 6). The methodology described in Sect. 3.1 can be repeated (adding noise as described in Sect. 2.3) and results can be averaged at an arbitrary distance. Figure 9 presents results of a single scan around side configuration across the West part of the Piedmont region for a total length of about 150 km (left panel). The reflectivity and Doppler velocity profiles (two top right panels) are averaged every 8 pulses, thus corresponding to an integration length of 1 km. Here, the high correlation estimator is selected. The black dashed line represents the height of the point hit by the boresight on the DEM surface, averaged over 8 samples. The Doppler profiles have been clipped to ± 8 m/s in order to show the presence of noise and deviations in the otherwise nearly flat profiles. For a better interpretation, the mean and standard deviation value of DEM elevation and NRCS are also added (two bottom right panels). They are computed by considering a square subgrid with side of 1 km, centred around the boresight axis and averaged every 8 samples along the ground track. These values are used later in the statistical analysis of Sect. 4, which considers a high number of scans similar to the one here presented.

In general, it can be seen that the reflectivity peaks closely follow the h_{bs} values (black dashed line in the top right panels),

200 which are also close to the DEM elevation mean values $\langle h_{DEM} \rangle$ (blue line in the third right panel), except in the regions with very marked orography (e.g. in the first 30 km of the scan). The clutter return generally drops below the single-pulse minimum detectable reflectivity of -18 dBZ at approximately $\pm 900\,\mathrm{m}$ from h_{bs}. Outside these heights the Doppler signal becomes increasingly noisy, practically reducing to a random number between $\pm$ the Nyquist velocity of 40 m/s at low SNR. The regions with significant deviations from the ideal flat reflectivity and Doppler profile correspond well to regions with

205 higher standard deviation in DEM height and NRCS.
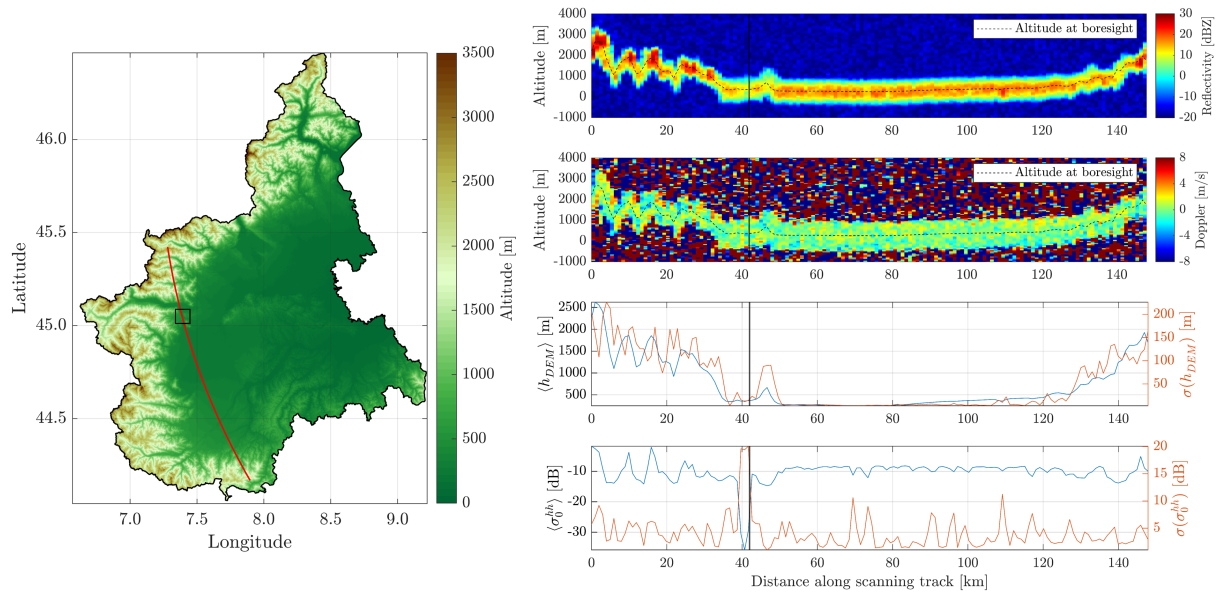
Figure 9. Case study of a continuous scan with the antenna scanning at the side of the satellite ground track. Left panel: the ground track of the antenna boresight (red line) with a counter-clockwise scanning across the Western Piedmont region with colors modulated by the orography. The black square corresponds to the region used in the single footprint case study (Sect. 3.1). Right panel: reflectivity (first row), Doppler velocity (second row), mean and standard deviation across the 1 km averaging region of elevation (third row) and NRCS (fourth row). The black vertical continuous lines represent the position of the single footprint case study seen in Sect. 3.1.
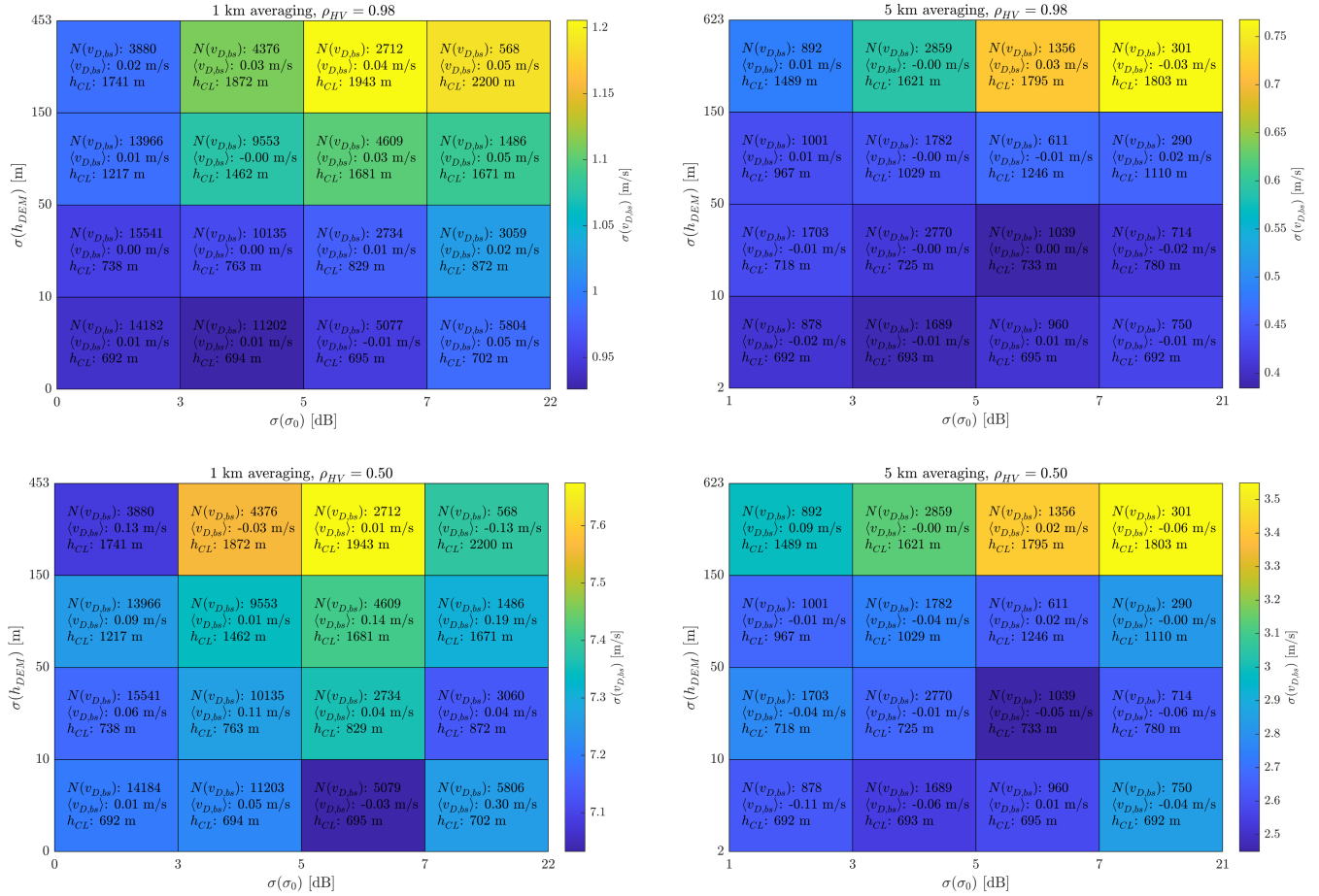
Figure 10. Boresight Doppler velocity statistical analysis for the four different cases: 1 km averaging, $\rho_{HV} = 0.98$ (top left); 5 km averaging, $\rho_{HV} = 0.98$ (top right); 1 km averaging, $\rho_{HV} = 0.5$ (bottom left); 5 km averaging, $\rho_{HV} = 0.5$ (bottom right). For each box corresponding to one of the 16 classes the color indicates the $\sigma(v_{D,bs})$ value. Inside each box, the number of occurrences $N(v_{D,bs})$, the mean value $\langle v_{D,bs} \rangle$, and the 95th percentile value of the clutter depth height h_{CL} are shown. The h_{CL} for the -18 dBZ level values have been computed using the averages of the ideal profiles rather than the noisy ones.

4 Statistical results

In order to capture a wide range of samples with different orography and inhomogeneity conditions, a large number of scans have been performed over the Piedmont region; along-track averages over 1 or 5 km (respectively 8 or 40 samples) have been performed. Each average produces a reflectivity and Doppler velocity profile in corrispondence with a DEM elevation and

210   NRCS mean and standard deviation value and an azimuth scanning angle.

4.1 Doppler velocity at boresight altitude: departures from 0 m/s

The boresight Doppler velocity value $v_{D,bs}$ is found as the value nearest to the height of the point hit by the antenna boresight. In presence of flat terrain and homogeneous surfaces, this value is expected to be zero, but noise, orography and NRCS variations across each footprint introduce departures. Four different cases have been studied, based on two different averaging distances (1 or 5 km) and two ρ_{HV} values (0.98 or 0.5). The larger the variability of the DEM height and NRCS within the averaging domain, the larger the departure from the 0 m/s reference. Therefore, by clustering profiles based on four standard deviations of the DEM height [1) $\sigma(h_{DEM}) < 10$; 2) $10 \leq \sigma(h_{DEM}) < 50$; 3) $50 \leq \sigma(h_{DEM}) < 150$; 4) $\sigma(h_{DEM}) < 450$] and four NRCS standard deviations [1) $\sigma(\sigma_0) < 3$; 2) $3 \leq \sigma(\sigma_0) < 5$; 3) $5 \leq \sigma(\sigma_0) < 7$; 4) $\sigma(\sigma_0) < 25$], 16 different classes have been identified and histograms for $v_{D,bs}$ for each class have been built. Results are reported in Fig. 10 for the four cases. Few considerations can be drawn.

- The classes have been chosen in order to include a sensible amount of occurrences, but in general classes with lower elevation standard deviation are higher in number due to the predominantly flat nature of the considered region.

- As expected, because of the different viewing geometry included in the database, the mean values of all the histograms, $\langle v_{D,bs} \rangle$, is close to 0 m/s for all classes. This confirms the fact that the surface can be used for calibrating the Doppler signal but in some cases only after substantial averaging.

- The standard deviation of the histograms, $\sigma(v_{D,bs})$, generally increases when moving towards higher DEM height and NRCS standard deviations.

- In presence of almost flat and homogeneous surfaces (bottom left pixels) $\sigma(v_{D,bs})$ is dominated by the noise. This baseline value heavily depends on the correlation ρ_{HV} and the averaging distance. $\rho_{HV} = 0.5$ produces extremely noisy Doppler velocities with a baseline exceeding 7 m/s. Only after 5 km averaging this can be brought down to 2.5 m/s. The high correlation value $\rho_{HV} = 0.98$ (which implies getting the surface Doppler velocity via the ghost processing) produces much better results and seems very promising.

- The effect of orography and NRCS inhomogeneity can be seen only when moving towards large values of higher standard deviations, while at lower standard deviations noise dominates and essentially defines the lower bound for $\sigma(v_{D,bs})$.

4.2 CFAD

Contour Frequency Altitude Display (CFAD) plots have been computed to show the variability of the reflectivity and Doppler velocity profiles when having a given variability of the DEM and NRCS across the integration zone (Fig. 11). For illustrative purposes, the case with $\rho_{HV} = 0.98$ and averaging over 1 km has been chosen for only two classes: 1) in the left column, almost perfectly flat regions with homogeneous NRCS (corresponding to the bottom left box of panels in Fig. 10); 2) in the right column, regions with very mountainous terrain and strong inhomogeneous NRCS (corresponding to the top right box of panels in Fig. 10). For Doppler velocities, a division based on ϕ_A was adopted, as the shape of the profiles change based on the
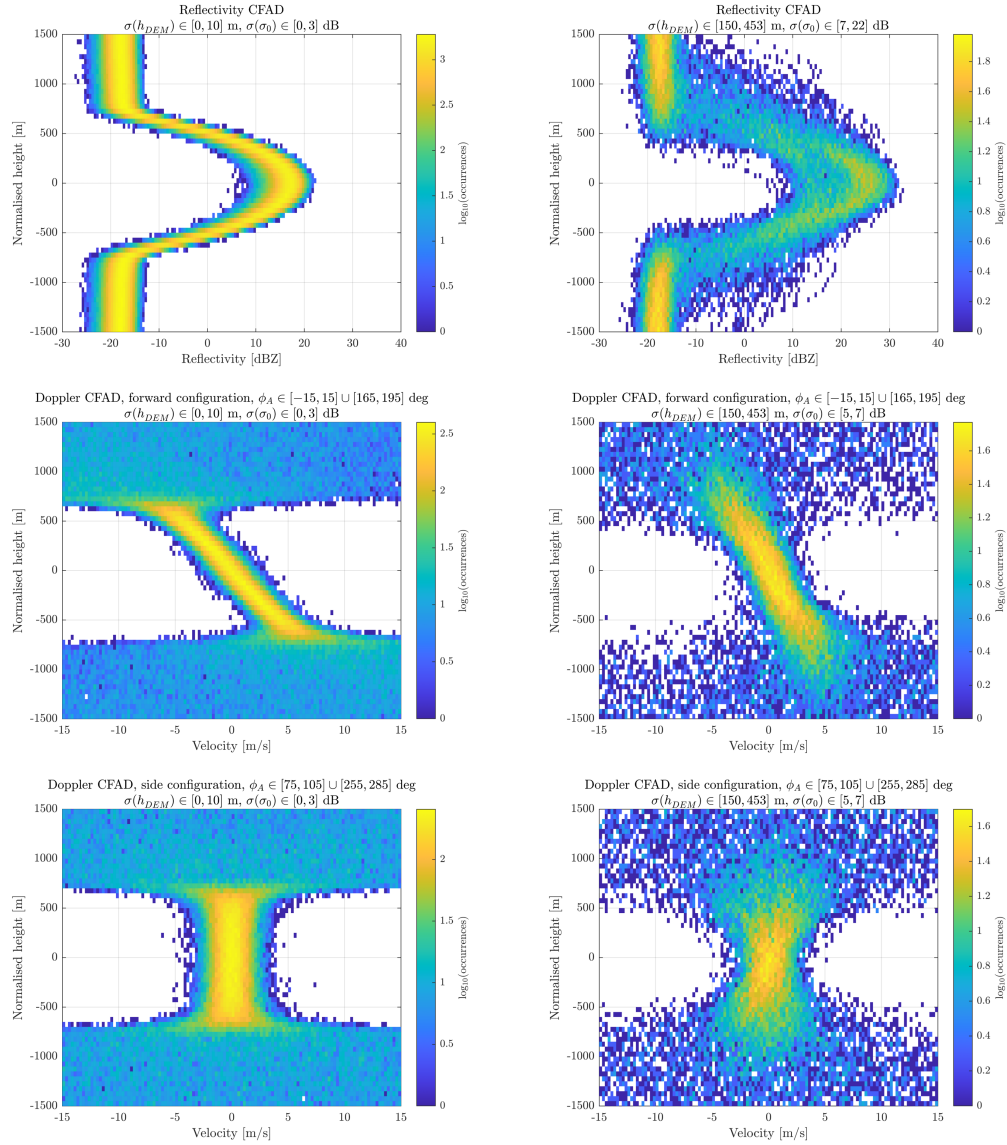
Figure 11. CFADs for reflectivity and Doppler, height is normalized by subtracting the boresight height h_{bs}, which is the height of the intersection between the boresight axis and the discretised surface defined by the DEM. On the left column we have the CFADs for the lowest standard deviation class, on the right for the highest. Top row: reflectivity CFADs. Middle row: Doppler velocity CFADs for forward configurations (profiles around $\phi_A = 180°$ are grouped together with those around $\phi_A = 0°$ changed in sign). Bottom row: Doppler velocity CFADs for side configuration.

antenna rotation angle. All CFADs have been rescaled to a rinormalised height so that h_{bs} is set to 0 m height.

In general, for almost flat and homogeneous surfaces (left panels), envelopes are more compact and they tend to behave similarly to the perfectly flat terrain (Scarsi et al., 2024) with the characteristic shape of the Doppler profiles for azimuth near

to forward/backward (centre left panel) and side view (bottom left panel) whereas when increasing DEM elevation and NRCS variability (right panels), profiles present larger spread. For instance, in the first row, reflectivities drop below the single-pulse minimum detectable value of approximately -18 dBZ at about 700 m in the left panel rather than at much larger values in the right panel. For the different classes, h_{CL} the height above surface at which 95% of the clutter profiles have reflectivity (without any noise) lower than -18 dBZ has been computed and is indicated as the third number in the boxes of Fig. 10. Results clearly show how the clutter region moves from 700 m in presence of flat terrain to more than 2 km in compex orography conditions.

Similarly, the inclination of the Doppler profiles near forward/backward looks (second row) becomes less pronounced but more scattered in presence of orography and NUBF.

5   Summary and conclusions

In this study, a novel simulator was developed to reproduce the clutter reflectivity and the Doppler velocity signal as expected for a spaceborne scanning Doppler radar instrument. The simulator is based on the ray-tracing approach with surface properties (slope, elevation, NRCS) derived from a high-resolution raster DEM and land classification map. A look-up table based on ground-based measurements is used to compute the normalised radar cross section (NRCS), σ_0. The simulator has been applied to the WIVERN mission, one of the two remaining candidates within the ESA's Earth Explorer 11 programme, which proposes the use of a conically scanning W-band Doppler radar to study in-cloud winds and the micro- and macro-physical properties of clouds and precipitation.

The simulator allows the characterisation of the expected ground return over regions with known terrain characteristics. In this study, an example of application is shown over the Piedmont region of Italy, which offers a variety of different scenes due to the presence of the Alps to the north and west and the flat regions of the Po valley. The presence of surface orography and the inhomogeneity of the backscatter cross sections within the radar footprint cause significant deviations from the reference provided by a homogeneous and flat surface. These effects have been demonstrated by the choice of a case study over a lake shore with nearby orography, where the NUBF phenomenon could be discussed in detail.

Furthermore, the simulator has been used for statistical analysis to examine the effect of elevation and NRCS variability over a large number of scans. In particular, departures from the 0 m/s Doppler velocity at boresight have been discussed as a function of the integration length and the variability of h_{DEM} and σ_0 within the integrating region. These results can be used to better assess over which regions and over which integration length the surface Doppler can be exploited for Doppler calibration purposes. Also they demonstrate that, over relatively flat vegetated surfaces, the clutter reflectivity of the surface can remain below low reflectivities ($< -20\,\mathrm{dBZ}$) for all heights more than 1 km above the ground. The situation becomes much worse over mountainous ranges and in presence of rocks and bare soil.

Future work should address improvements to the σ_0 dataset as a function of incidence angle and land type; additional field campaign measurements with ground-based radars are strongly recommended. Further applications of this tool are possible for missions with nadir-pointing radar instruments, as for the EarthCARE and CloudSat Cloud Profiling Radars (Tanelli et al.,

2008; Illingworth et al., 2015; Kollias et al., 2023), or cross-track scanning, as for the Global Precipitation Measuring Dual Precipitation Radar (Skofronick-Jackson et al., 2016).

Code and data availability. Simulator code and all raw data are available upon request. The ASTER GDEM dataset is freely available
280   subject to registration from NASA servers (https://asterweb.jpl.nasa.gov/GDEM.asp, Abrams et al. (2010)).

Author contributions. FM performed most of the simulations and the analyses. AB contributed to the analysis, the writing and has defined the project. PK contributed to the discussion and the review of the paper.

Competing interests. At least one of the (co-)authors is a member of the editorial board of *Atmospheric Measurement Techniques*.

Acknowledgements. This research has been supported by the European Space Agency under the activities "WInd VElocity Radar Nepho-
285   scope (WIVERN) Phase A Science and Requirements Consolidation Study" (ESA Contract Number RFP/3-18420/24/NL/IB/ab) and by the Italian Space Agency (ASI) project "Scientific studies for the Wind Velociy Radar Nephoscope (WIVERN) mission" (Project number: 2023-44-HH.0). This research used the Mafalda cluster at Politecnico di Torino.

References

Abrams, M., Bailey, B., Tsu, H., and Hato, M.: The aster global dem, Photogrammetric Engineering and Remote Sensing, 76, 344–348,
290   2010.

Battaglia, A. and Kollias, P.: Impact of Receiver Saturation on Surface Doppler velocity measurements from the EarthCARE Cloud Profiling
Radar, IEEE Trans. Geosci. Remote Sens., 53, doi 10.1109/TGRS.2014.233589, 2014.

Battaglia, A., Tanelli, S., and Kollias, P.: Polarization Diversity for Millimeter Spaceborne Doppler Radars: An Answer for Observing Deep
Convection?, J. Atmos. Ocean Technol., 30, 2768–2787, https://doi.org/10.1175/JTECH-D-13-00085.1, 2013.

295   Battaglia, A., Westbrook, C. D., Kneifel, S., Kollias, P., Humpage, N., Löhnert, U., Tyynelä, J., and Petty, G. W.: G band atmospheric radars:
new frontiers in cloud physics, Atm. Meas. Tech., 7, 1527–1546, https://doi.org/10.5194/amt-7-1527-2014, 2014.

Battaglia, A., Wolde, M., D'Adderio, L. P., Nguyen, C., Fois, F., Illingworth, A., and Midthassel, R.: Characterization of Surface Radar Cross
Sections at W-Band at Moderate Incidence Angles, IEEE Trans. Geosci. Remote Sens., 55, 3846–3859, 10.1109/TGRS.2017.2682423,
2017.

300   Battaglia, A., Kollias, P., Dhillon, R., Roy, R., Tanelli, S., Lamer, K., Grecu, M., Lebsock, M., Watters, D., Mroz, K., Heymsfield, G., Li,
L., and Furukawa, K.: Spaceborne Cloud and Precipitation Radars: Status, Challenges, and Ways Forward, Reviews of Geophysics, 58,
e2019RG000 686, https://doi.org/10.1029/2019RG000686, e2019RG000686 10.1029/2019RG000686, 2020.

Battaglia, A., Martire, P., Caubet, E., Phalippou, L., Stesina, F., Kollias, P., and Illingworth, A.: End to end simulator for the WIVERN
W-band Doppler conically scanning spaceborne radar, Atm. Meas. Tech., 2021, 1–31, https://doi.org/10.5194/amt-2021-342, 2022.

305   Battaglia, A., Rizik, A., Tridon, F., and Isakeneta, I.: I and Qs simulation and processing envisaged for space-borne polarisation Diversity
Doppler Radars, IEEE Trans. Geosci. Remote Sens., submitted, 2024.

Burns, D., Kollias, P., Tatarevic, A., Battaglia, A., and Tanelli, S.: The performance of the EarthCARE Cloud Profiling Radar in marine
stratiform clouds, J. Geophys. Res. Atm., 121, 14,525–14,537, https://doi.org/10.1002/2016JD025090, 2016.

Delrieu, G., Creutin, J. D., and Andrieu, H.: Simulation of Radar Mountain Returns Using a Digitized Terrain Model, J. Atmos. Ocean
310   Technol., 12, 1038 – 1049, https://doi.org/10.1175/1520-0426(1995)012<1038:SORMRU>2.0.CO;2, 1995.

Durden, S. L., Tanelli, S., and Dobrowalski, G.: CloudSat W-Band Radar Measurements of Surface Backscatter, IEEE Geosci. Remote Sens.
Lett., 8, 401–405, 2011.

ESA-WIVERN-Team: WIVERN   Report   for   Assessment,   Tech.   rep.,   ESA-EOPSM-WIVE-RP-4375,   available   at
https://eo4society.esa.int/event/earth-explorer-11-user-consultation-meeting/, 2023.

315   Fabry, F.: Radar Meteorology: Principles and Practice, Cambridge University Press, https://doi.org/10.1017/CBO9781107707405, 2015.

Gabella, M. and Perona, G.: Simulation of the Orographic Influence on Weather Radar Using a Geometric–Optics Approach, J. Atmos.
Ocean Technol., 15, 1485 – 1494, https://doi.org/10.1175/1520-0426(1998)015<1485:SOTOIO>2.0.CO;2, 1998.

Gabella, M., Notarpietro, R., Turso, S., and Perona, G.: Simulated and measured X-band radar reflectivity of land in mountainous terrain
using a fan-beam antenna, International Journal of Remote Sensing, 29, 2869–2878, https://doi.org/10.1080/01431160701596149, 2008.

320   Illingworth, A. J., Barker, H. W., Beljaars, A., Ceccaldi, M., Chepfer, H., Clerbaux, N., Cole, J., Delanoë, J., Domenech, C., Donovan, D. P.,
Fukuda, S., Hirakata, M., Hogan, R. J., Huenerbein, A., Kollias, P., Kubota, T., Nakajima, T., Nakajima, T. Y., Nishizawa, T., Ohno, Y.,
Okamoto, H., Oki, R., Sato, K., Satoh, M., Shephard, M. W., Velázquez-Blázquez, A., Wandinger, U., Wehr, T., and van Zadelhoff, G.-J.:
The EarthCARE Satellite: The Next Step Forward in Global Measurements of Clouds, Aerosols, Precipitation, and Radiation, Bull. Amer.
Met. Soc., 96, 1311–1332, https://doi.org/10.1175/BAMS-D-12-00227.1, 2015.

325 Illingworth, A. J., Battaglia, A., Bradford, J., Forsythe, M., Joe, P., Kollias, P., Lean, K., Lori, M., Mahfouf, J.-F., Melo, S., Midthassel, R., Munro, Y., Nicol, J., Potthast, R., Rennie, M., Stein, T. H. M., Tanelli, S., Tridon, F., Walden, C. J., and Wolde, M.: WIVERN: A New Satellite Concept to Provide Global In-Cloud Winds, Precipitation, and Cloud Properties, Bull. Amer. Met. Soc., 99, 1669–1687, https://doi.org/10.1175/BAMS-D-16-0047.1, 2018.

Kollias, P., Battaglia, A., Lamer, K., Treserras, B. P., and Braun, S. A.: Mind the Gap - Part 3: Doppler Velocity Measurements From Space,
330 Frontiers in Remote Sensing, 3, https://doi.org/10.3389/frsen.2022.860284, 2022.

Kollias, P., Puidgomènech Treserras, B., Battaglia, A., Borque, P. C., and Tatarevic, A.: Processing reflectivity and Doppler velocity from EarthCARE's cloud-profiling radar: the C-FMR, C-CD and C-APC products, Atmospheric Measurement Techniques, 16, 1901–1914, https://doi.org/10.5194/amt-16-1901-2023, 2023.

Kummerow, C., Barnes, W., Kozu, T., Shiue, J., and Simpson, J.: The Tropical Rainfall Measuring Mission (TRMM) Sensor Package, J.
335 Atmos. Ocean Technol., 15, 809–817, https://doi.org/10.1175/1520-0426(1998)015<0809:TTRMMT>2.0.CO;2, 1998.

Lamer, K., Kollias, P., Battaglia, A., and Preval, S.: Mind the gap – Part 1: Accurately locating warm marine boundary layer clouds and precipitation using spaceborne radars, Atm. Meas. Tech., 13, 2363–2379, https://doi.org/10.5194/amt-13-2363-2020, 2020.

Li, L., Heymsfield, G., McLinden, M., Racette, P., Cooley, M., Stenger, P., and Spence, T.: Spaceborne Atmospheric Radar Technology Development, in: 2020 IEEE Radar Conference (RadarConf20), pp. 1–4, https://doi.org/10.1109/RadarConf2043947.2020.9266464, 2020.

340 Maahn, M., Burgard, C., Crewell, S., Gorodetskaya, I. V., Kneifel, S., Lhermitte, S., Tricht, K. V., and van Lipzig, N. P. M.: How does the spaceborne radar blind zone affect derived surface snowfall statistics in polar regions?, J. Geophys. Res. Atm., 119, 13 604–13 620, doi:10.1002/2014JD022079, 2014.

Meneghini, R. and Kozu, T.: Spaceborne weather radar, Artech House, 1990.

Meneghini, R., Iguchi, T., Kozu, T., Liao, L., Okamoto, K., Jones, J. A., and Kwiatkowski, J.: Use of the Surface Reference Technique
345 for Path Attenuation Estimates from the TRMM Precipitation Radar, J. Appl. Meteorol., 39, 2053–2070, https://doi.org/10.1175/1520-0450(2001)040<2053:UOTSRT>2.0.CO;2, 2000.

Pazmany, A. L., Galloway, J. C., Mead, J. B., Popstefanija, I., McIntosh, R. E., and Bluestein, H. W.: Polarization Diversity Pulse-Pair Technique for Millimeter-WaveDoppler Radar Measurements of Severe Storm Features, J. Atmos. Ocean Technol., 16, 1900–1911, https://doi.org/10.1175/1520-0426(1999)016<1900:PDPPTF>2.0.CO;2, 1999.

350 Puigdomènech Treserras, B. and Kollias, P.: An Improved Geolocation Methodology for Spaceborne Radar and Lidar Systems, EGUsphere, 2024, 1–25, https://doi.org/10.5194/egusphere-2024-1546, 2024.

Rizik, A., Battaglia, A., Tridon, F., Scarsi, F. E., Kötsche, A., Kalesse-Los, H., Maahn, M., and Illingworth, A.: Impact of Crosstalk on Reflectivity and Doppler Measurements for the WIVERN Polarization Diversity Doppler Radar, IEEE Transactions on Geoscience and Remote Sensing, 61, 1–14, https://doi.org/10.1109/TGRS.2023.3320287, 2023.

355 Scarsi, F. E., Battaglia, A., Tridon, F., Martire, P., Dhillon, R., and Illingworth, A.: Mispointing characterization and Doppler velocity correction for the conically scanning WIVERN Doppler radar, Atm. Meas. Tech., 17, 499–514, https://doi.org/10.5194/amt-17-499-2024, 2024.

Schutgens, N. A. J.: Simulating Range Oversampled Doppler Radar Profiles of Inhomogeneous Targets, J. Atmos. Ocean Technol., 25, 26–42, doi: 10.1175/2007JTECHA956.1, 2008.

360 Skofronick-Jackson, G., Petersen, W., Berg, W., Kidd, C., Stocker, E., Kirschbaum, D., Kakar, R., Braun, S., Huffman, G., Iguchi, T., Kirstetter, P., Kummerow, C., Meneghini, R., Oki, R., Olson, W., Takayabu, Y., Furukawa, K., and Wilheit, T.: The Global Precipitation Measurement (GPM) Mission for Science and Society, Bull. Amer. Met. Soc., doi:10.1175/BAMS-D-15-00306.1, 2016.

Stephens, G., Winker, D., Pelon, J., Trepte, C., Vane, D., Yuhas, C., L'Ecuyer, T., and Lebsock, M.: CloudSat and CALIPSO within the A-Train: Ten Years of Actively Observing the Earth System, Bull. Amer. Met. Soc., 99, 569–581, https://doi.org/10.1175/BAMS-D-16-0324.1, 2018.

Tanelli, S., Im, E., Durden, S. L., Facheris, L., and Giuli, D.: The Effects of Nonuniform Beam Filling on Vertical Rainfall Velocity Measurements with a Spaceborne Doppler Radar, J. Atmos. Ocean Technol., 19, 1019–1034, https://doi.org/10.1175/1520-0426(2002)019<1019:TEONBF>2.0.CO;2, 2002.

Tanelli, S., Durden, S. L., Im, E., Pak, K. S., Reinke, D. G., Partain, P., Haynes, J. M., and Marchand, R. T.: CloudSat's Cloud Profiling Radar After Two Years in Orbit: Performance, Calibration, and Processing, IEEE Trans. Geosci. Remote Sens., 46, 3560–3573, https://doi.org/10.1109/TGRS.2008.2002030, 2008.

Tanelli, S., Durden, S. L., and Johnson, M. P.: Airborne Demonstration of DPCA for Velocity Measurements of Distributed Targets, IEEE Geosci. Remote Sens. Lett., 13, 1415–1419, https://doi.org/10.1109/LGRS.2016.2581174, 2016.

Ulaby, F. T. and Dodson, M. C.: Handbook of Radar Scattering Statistics for Terrain, Remote Sensing Library, Artech House, Norwood, MA, hardcover, 1991.

Wolde, M., Battaglia, A., Nguyen, C., Pazmany, A. L., and Illingworth, A.: Implementation of polarization diversity pulse-pair technique using airborne W-band radar, Atm. Meas. Tech., 12, 253–269, https://doi.org/10.5194/amt-12-253-2019, 2019.